AIAA JOURNAL
Vol. 47, No. 5, May 2009

Rotational and Vibrational Temperature Distributions for a Dielectric Barrier Discharge in Air

Scott A. Stanfield* and James Menart†
Wright State University, Dayton, Ohio, 45435
and
Charles DeJoseph Jr.,‡ Roger L. Kimmel,§ and James R. Hayes¶
U.S. Air Force Research Laboratory, Wright–Patterson Air Force Base, Ohio, 45433

DOI: 10.2514/1.37648

Spatially resolved rotational and vibrational temperatures for N_2 and rotational temperatures for N_2^+, as a function of voltage, have been obtained for an asymmetric surface mode dielectric barrier discharge using emission spectroscopy. The rotational temperatures were obtained from a nonlinear least-squares fit of a two-temperature theoretical spectrum with the measured spectra of the $N_2(C^3\Pi_u - B^3\Pi_g)$ and $N_2^+(B^2\Sigma_u^+ - X^2\Sigma_g^+)$ electronic band systems. The vibrational temperatures were obtained by applying the Boltzmann plot method to the $\Delta v = -2$ sequence of the $N_2(C^3\Pi_u - B^3\Pi_g)$ electronic band system. It was observed that the rotational temperatures for N_2 and N_2^+ decreased in the induced flow direction and increased with increasing voltage. Values started at 390 ± 10 K and decreased to 340 ± 10 K for N_2 and started at 500 ± 15 K and decreased to 450 ± 15 K for N_2^+. The vibrational temperatures also decreased in the induced flow direction from 3250 to 2850 ± 300 K. A difference in rotational temperatures between N_2 and N_2^+ was observed for all voltages studied, and these differences increased with increasing voltage. The rotational temperatures of both species fluctuated in the spanwise direction. These fluctuations damped out in the streamwise direction and were weakly correlated with the attachment points of the microdischarges on the edge of the exposed electrode.

Nomenclature

$A_{v'}^{v''}$	=	Einstein coefficient for a vibrational transition
$A_{v',J'}^{v'',J''}$	=	Einstein coefficient for a rovibrational transition
c	=	speed of light
d	=	diameter of fiber bundle
D_{eff}	=	effective diameter of lens
$F_{J'}$	=	rotational energy of the J' energy level
f_1	=	focal length of front lens
f_2	=	focal length of back lens
g	=	gap distance between lens 1 and lens 2
$g_{J'}$	=	degeneracy of the J' energy level
$G(v')$	=	energy of the v' energy level
h	=	Planck's constant
$I_{v',J'}^{v'',J''}$	=	intensity of a rovibrational line
J'	=	upper-state rotational quantum number
J''	=	lower-state rotational quantum number
k	=	Boltzmann constant
L	=	plasma depth
$L_{v'}^{v''}$	=	theoretical vibrational band
$L_{J',v'}^{J'',v''}$	=	theoretical rotational line
M_A	=	magnification at location A
M_B	=	magnification at location B
n	=	total number of data points
N_{Fit}	=	number of fit parameters
$N_{v'}$	=	number of molecules in the v' vibrational level
$N_{v',J'}$	=	number of molecules in the v' and J' energy level
$P(\lambda, \lambda')$	=	instrumental line shape
Q_r	=	rotational partition function
Q_v	=	vibrational partition function
$S_{J'}^{J''}$	=	rotational line strength
T	=	temperature
T_{rot}	=	rotational temperature
T_{vib}	=	vibrational temperature
v'	=	upper-state vibrational quantum number
v''	=	lower-state vibrational quantum number
$W_{v'}^{v''}(\lambda)$	=	spectral line
y_i	=	measured data point
$y(x_i)$	=	fit to the measured data point
$y_e\omega_e$	=	spectroscopic constant
θ	=	collection cone angle
λ	=	wavelength
$\lambda_{v',J'}^{v'',J''}$	=	wavelength of a rovibrational line
σ_i^2	=	standard deviation of the noise in the measurement
$\Phi(\lambda, \lambda_{v',J'}^{v'',J''})$	=	line shape function
χ^2	=	chi squared statistical parameter
χ_R^2	=	normalized chi squared called reduced chi squared
ω_e	=	spectroscopic constant
$\omega_e\chi_e$	=	spectroscopic constant

Presented as Paper 3876 at the 38th AIAA Plasmadynamics and Lasers Conference in conjunction with the 16th International Conference on MHD Energy Conversion, Miami, FL, 25–28 June 2007; received 20 March 2008; revision received 27 October 2008; accepted for publication 7 November 2008.

*Ph.D. Candidate, Department of Mechanical and Materials Engineering; stanfield.3@wright.edu. Member AIAA.
†Associate Professor, Department of Mechanical and Materials Engineering; james.menart@wright.edu. Associate Fellow AIAA.
‡Principal Research Physicist.
§Principal Aerospace Engineer. Associate Fellow AIAA.
¶Senior Research Engineer.

I. Introduction

ASYMMETRIC surface mode dielectric barrier discharges (ASDBDs) can be used as flow control devices that, through momentum coupling, are capable of altering the gas flow around them [1]. This simple promising concept has spurred an abundance of work needed in developing a quantitative and qualitative understanding necessary for the applications of ASDBDs to flow control. It has been shown that ASDBDs are capable of suppressing flow separation [2–5], controlling the boundary layer [6], aiding lift

enhancement and roll-control [7], controlling the wake of a circular cylinder [8,9], reducing drag [10], and influencing lift and controlling flow separation for micro air vehicles [11]. Modeling work on the fundamental operation of an ASDBD has also been done [12–21]. Other studies have shown the effect of ASDBDs on the electrode surface [22], studied the chemical kinetics [23,24], measured the induced velocity [25–27], measured the thrust produced [28,29], studied the effects of operating frequency on efficiency [30], and studied the fundamental operations of the device [1,31–33].

Because dielectric barrier discharges (DBD) have a number of promising uses, it is important that the fundamentals are understood. In this paper, the rotational and vibrational temperatures for an ASDBD, which is a particular type of DBD, are determined by means of emission spectroscopy. Emission spectroscopy has been used to determine the rotational and vibrational temperatures for a variety of gas mixtures; however, there has been little work with pure air, and no attempts have been made to spatially resolve these temperatures within the discharge [34–41]. This work is the first to provide spatial resolved rotational and vibrational temperature profiles in an air ASDBD.

Chipper et al. [34] conducted spectroscopic studies for a planar dielectric barrier discharge (PDBD) operating in He/Air and He/N_2 gas mixtures. The electrodes in a PDBD are parallel, separated by a gap and insulated with a dielectric material. They used emission spectroscopy to determine the rotational temperature from a Boltzmann plot of the $B^2\Sigma_u^+ - X^2\Sigma_g^+$ electronic band system of N_2^+ as a function of the ratio of N_2 and He flow rates. They report rotational temperatures ranging from 400 to 440 K depending on flow conditions. In their work, the presence of He significantly altered the discharge by aiding ionization through Penning ionization reactions. The inclusion of Penning ionization causes a larger plasma density, which leads to a more diffuse discharge [35]. This type of discharge is ideal for surface treating applications at atmospheric pressure. Luque et al. [36] investigated PDBDs operating in CH_4/CO_2 gas mixtures and determined the rotational temperature at a single location within the discharge. The rotational temperature was determined from a Boltzmann plot of the $A^2\Delta - X^2\Pi$ electronic band system of CH. Motret et al. [37] used emission spectroscopy to determine the rotational temperature within a PDBD operating in an environment composed of argon and water vapor. They obtained the rotational temperature from OH by using the Boltzmann plot method and found this temperature to be 450 ± 10 K. Pellerin et al. [38] determined the rotational temperature in a PDBD operating in an environment composed of argon and CF_4. They determined this temperature from the $A^3\Pi_g - X'^3\Pi_u$ electronic band system of C_2 by numerically minimizing χ^2. Tomai et al. [39] used the same electronic band system and method for determining temperature as Pellerin et al. [38] for a PDBD operating in an environment of CO_2. Nersisyan and Graham [40] measured the rotational and vibrational temperature from the $B^2\Sigma_u^+ - X^2\Sigma_g^+$ and $C^3\Pi_u - B^3\Pi_g$ electronic band systems of N_2^+ and N_2, respectively, within a PDBD operating in air with helium flowing through the interelectrode gap. The rotational and vibrational temperatures were found to be 360 ± 20 and 2700 ± 900 K, respectively, by minimizing χ^2. Bibinov et al. [35], determined the rotational temperature for a PDBD operating in a He/N_2 environment by comparing the measured spectra with a calculated spectra. They found a rotational temperature for N_2 and N_2^+ to be 310 ± 10 and 600 K, respectively. It was also determined that the rotational temperature for N_2 remained constant as a function of the nitrogen partial pressure, whereas N_2^+ did not. In their work, the total pressure remained constant at 1 atm. They attributed this nonequilibrium phenomena to the long-lived metastable species N_2 $(A^3\Sigma_u^+)$, which in a mixture of N_2/He is not easily quenched. It was also concluded that the rotational temperature carries information about the influence of metastable reactions on the chemical kinetics in DBDs. Stefanovic et al. [42] showed a similar discrepancy between the rotational temperature of N_2 and N_2^+ as observed by Bibinov et al. [35] for a PDBD operating in air at atmospheric pressure. His results will be discussed later on in Sec. V. In all the cases mentioned, the DBD studied had a different configuration than that used for flow control applications.

The only investigation found to make rotational and vibrational temperature measurements in an ASDBD, operating in pure air, is Borghi et al. [41]. Borghi et al. measured the rotational temperature as a function of frequency and the vibrational temperature as a function of voltage and frequency. They show that the rotational temperature increases with increasing frequency from 290 to 375 K, and the vibrational temperature increases from 3400 to 3800 K. In this case, as well as all the measurements made in nonpure air DBDs described in the preceding paragraph, no attempts were made to spatially determine the rotational or vibrational temperatures within the DBD. In this paper, spatially resolved rotational and vibrational temperatures are presented for ASDBDs operating in atmospheric air, which is important for aerodynamic applications.

In this work, emission spectroscopy is used to map the rotational and vibrational temperatures of the discharge region for an ASDBD operating in atmospheric air at an ambient temperature of 295 K. The temperatures are obtained from the $C^3\Pi_u - B^3\Pi_g$ electronic band system of N_2 and from the $B^2\Sigma_u^+ - X^2\Sigma_g^+$ electronic band system of N_2^+. The translational temperature is inferred from the measured N_2 rotational temperature by assuming the two are in equilibrium. This is a valid assumption at the temperatures and pressure involved in this work because the rotational energy levels are closely spaced and allow for rapid energy transfer between the two energy modes [43]. The rotational temperatures are obtained from a two-temperature fit by numerically comparing the measured spectra of the 0–1, 0–2, 1–3, 2–4, 3–5, 0–3, 1–4, 2–5, 3–6, 4–7, and 4–8 vibrational transitions of N_2 and the 0–0 and 1–1 vibrational transitions of N_2^+ to calculated spectra. The comparisons were done quantitatively using the statistical parameter χ_R^2, which was minimized iteratively by adjusting the fitting parameters using a program called N2SPECFIT [44,45]. Each of the two rotational temperatures obtained (one for N_2 and one for N_2^+) corresponds to the calculated spectrum that best matches the measured spectrum. This method has been used successfully in the past to determine the thermal boundary layer of a DC glow discharge on top of a flat plate in a Mach 5 flow [45]. The vibrational temperature was obtained from a Boltzmann plot of the relative upper vibrational state number densities for N_2 determined by N2SPECFIT.

II. Experimental Facilities

The ASDBD, experimental facilities, and the experimental setup are given in the following two subsections.

A. Asymmetric Surface Mode Dielectric Barrier Discharge

The ASDBD used in this work is shown in Fig. 1 and consists of two copper electrodes; one exposed and one insulated beneath a 1-mm-thick glass plate. As can be seen from Fig. 1, there is a 2 mm

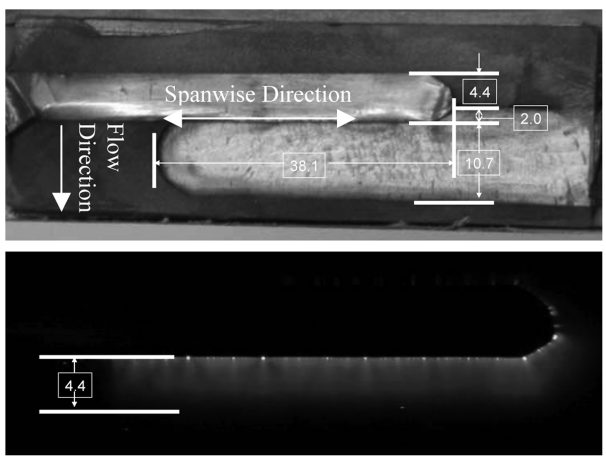

Fig. 1 Electrodes shown with and without a DBD. The glow is over the encapsulated electrode. All dimensions are in millimeters.

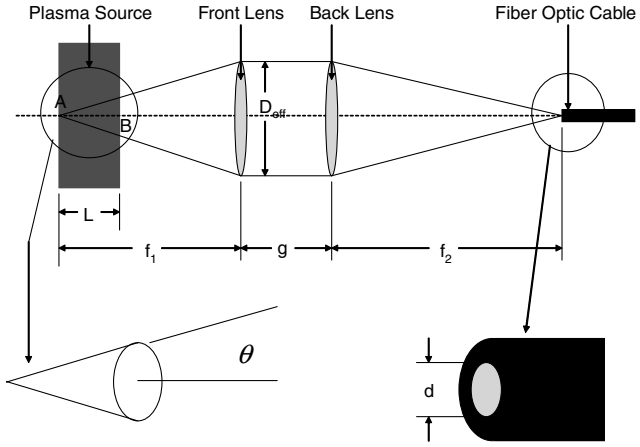

Fig. 2 Optical collection system.

overlap between the exposed and encapsulated electrode. This was done to reduce arcing. The width of the encapsulated electrode is 10.7 mm, and the width of the exposed electrode is 4.4 mm. The length of the region where the electrodes overlap in the spanwise direction is 38.1 mm.

A discharge is established over the encapsulated electrode by placing an oscillating voltage of sufficient strength between the two electrodes. An induced flow, moving across the encapsulated electrode and away from the exposed electrode, is generated as a result of the asymmetry of the electrodes. The asymmetry is crucial because it results in the ions having a nonzero net momentum flux. The net momentum flux is imparted to the neutrals by collisions inducing a flow. The phenomena responsible for establishing the induced flow is known as an electrohydrodynamic (EHD) effect.

The voltage and current of the ASDBD are measured with an oscilloscope. In this work a sinusoidal voltage at 5000 Hz is applied to the exposed electrode, and the encapsulated electrode is grounded. Four different peak-to-peak voltages were used: 8000, 9600, 11200, and 12800 V. An Agilent 33220A function generator produces the initial voltage waveform and sends it to a Crown CE1000 power supply via a BNC connection. The function generator is capable of many different waveforms including those specified by the user and has a maximum peak-to-peak voltage output of 5 V. The power supply voltage output is further amplified with a Corona Magnetics Inc CMI-5012 step-up transformer. The transformer is directly attached to the DBD and is capable of delivering up to 20 kV at 5 kHz. The voltage waveform is measured using a Tektronix P6015A high-voltage probe and is connected to a Tektronix TDS 3034B oscilloscope with a BNC cable. The high-voltage probe is capable of measuring peak-to-peak voltages up to 20 kV and has a bandwidth of 75 MHz. The discharge current is obtained by measuring the voltage drop across a 100 Ohm resister with a Tektronix P6139A probe. Both probes are designed for the oscilloscope and are properly compensated.

B. Collection Optics and Spectroscopic System

Figure 2 shows the optical collection system, which directs the emitted radiation from the ASDBD to the spectrometer and determines the spatial resolution of the measurements. It is important to know the dimensions of the collection volume because all measurements obtained are averages over this volume [45,46]. The emitted radiation from the DBD is collected and collimated by a Newport KBX250 biconvex lens with an effective focal length of 250 mm. The collimated radiation is focused with a Newport KBX1000 biconvex lens with an effective focal length of 1000 mm onto a Roper Scientific LG-455-020-1 fiber optic bundle. The fiber optic bundle channels the collected radiation into a $\frac{3}{4}$ meter Acton 2756 spectrometer where it is diffracted and focused onto an Andor DU 440-BU CCD camera. The spectrometer has a resolution of 0.023 nm at a wavelength of 435.8 nm using a grating of 1200 grooves per mm. The spectral response of the system was calibrated using a Newport 63976 tungsten halogen lamp. The magnification of the system is four resulting in a predicted spot size at locations A and B in Fig. 2 of 0.25 and 0.45 mm, respectively. The predicted dimensions are slightly smaller than the actual spot size because of aberrations and other optical inefficiencies. The entrance slit of the spectrometer has a height and width of 4 mm and 15 μm, respectively. It is assumed that any light gathered by the fiber optic bundle is delivered to the spectrometer.

III. Rotational Temperature Determination

The program N2SPECFIT is a procedural code used to analyze the measured spectra. It is capable of determining the rotational temperature for the first and second positive electronic band systems of N_2 and the first negative electronic band system of N_2^+, along with the upper-state number densities of the various bands within these band systems. The details of this code are given in [47]. The program assumes the rotational distribution is Boltzmann and calculates spectra for an initial rotational temperature. Note that no assumption is made about the vibrational distribution. The initial temperature is iterated along with the upper-state number density of each band until the numerical spectra matches the measured spectra. Comparison between the two spectra is done statistically with χ_R^2, and the converged solution corresponds to the minimum χ_R^2. Note, this can be done using a different rotational temperature for each electronic band system included in the fit. Figure 3 shows the agreement between one of the measured spectra from this work and the corresponding calculated spectra. The measured and calculated spectra essentially lie on top of one another indicating an accurate fit. The spectroscopic constants used by N2SPECFIT for this work are those tabulated by Gilmore et al. [48] and Laher and Gilmore [49].

The standard deviation of the noise, used in determining χ_R^2, is determined from a range in the measured spectra scan that has no spectral structure. The instrumental line shape used by N2SPECFIT is best approximated with a Gaussian distribution and was obtained by measuring and curve fitting the spectra of a mercury discharge tube for the transition at 435.833 nm.

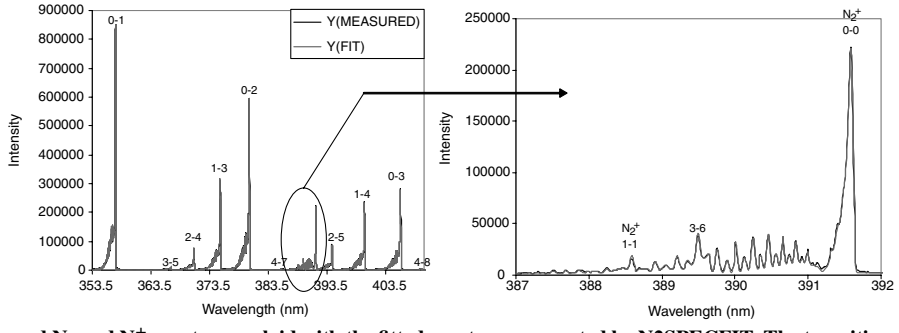

Fig. 3 Example of measured N_2 and N_2^+ spectra overlaid with the fitted spectrum generated by N2SPECFIT. The transitions of N_2^+ are labeled and all other transitions are for N_2. The transitions are labeled as v'-v'' above the band heads.

IV. Vibrational Temperature Measurement Technique

The Boltzmann plot method was applied to the 0–2, 1–3, and 2–4 vibrational transitions of the $C^3\Pi_u - B^3\Pi_g$ electronic band system of N_2 to obtain the vibrational temperature. The Boltzmann distribution for the vibrational energy levels are given as

$$\frac{N_{v'}}{N} = \frac{\exp(-\frac{G(v')hc}{kT_{\text{vib}}})}{Q_v} \tag{1}$$

where

$$G(v') = \left(v' + \tfrac{1}{2}\right)\omega'_e - \left(v' + \tfrac{1}{2}\right)^2 \chi'_e\omega'_e + \left(v' + \tfrac{1}{2}\right)^3 y'_e\omega'_e \ldots \tag{2}$$

The spectral response of the spectroscopic system has been accounted for with a relative calibration, which means that the measured spectral transitions need to be taken relative to another measured transition. In this work, the population distribution is relative to the $v' = 0$ energy level. The fraction of $N_{v'=0}$ is given as

$$\frac{N_{v'=0}}{N} = \frac{\exp(-\frac{G(v'=0)hc}{kT_{\text{vib}}})}{Q_v} \tag{3}$$

Dividing Eq. (1) by Eq. (3) gives

$$\frac{N_{v'}}{N_{v'=0}} = \exp\left[(G(v'=0) - G(v'))\frac{hc}{kT_{\text{vib}}}\right] \tag{4}$$

Taking the natural logarithm of both sides of Eq. (4) results in an equation of a line in the form $y = mx$

$$\ell_n\left(\frac{N_{v'}}{N_{v'=0}}\right) = \frac{1}{T_{\text{vib}}}\frac{(G(v'=0) - G(v'))hc}{k} \tag{5}$$

The vibrational temperature is determined by plotting $\ell_n(\frac{N_{v'}}{N_{v'=0}})$ vs $\frac{(G(v'=0)-G(v'))hc}{k}$ and setting the slope equal to $\frac{1}{T_{\text{vib}}}$. Error bars for vibrational temperature are determined by tracking the sensitivity of the uncertainty associated with measuring the upper-state number density ($N_{v'}$) using an uncertainty analysis on Eq. (5).

V. Results

Rotational and vibrational temperatures were measured throughout the discharge region of an ASDBD generated with a sinusoidal voltage for four different voltages at a frequency of 5000 Hz. The peak-to-peak voltages investigated were 8000, 9600, 11200, and 12800 V. The optical line of sight, as indicated in Fig. 4, was perpendicular to the electrodes (looking down on the electrodes) providing spatial resolution in the spanwise and flow directions of the ASDBD. The measurements were taken after the ASDBD ran for 30 min in order to reach a quasi-steady operational state.

Figure 4 shows the measured rotational and vibrational temperatures for the N_2 ($C^3\Pi_u - B^3\Pi_g$) electronic band system corresponding to an applied peak-to-peak voltage of 12,800 V. The rectangle with a dashed white perimeter indicates the region in the discharge where temperatures were measured. This region and the corresponding temperature contour profiles are one-to-one images. Each contour profile contains 152 measured points with spacing between points in the flow direction of 0.14 mm up to a location of 1.10 mm from the edge of the exposed electrode, after which the spacing is increased to 0.28 mm. The spacing in the spanwise direction is 3.17 mm. The rotational temperature results show the rotational temperature is greatest where the exposed and encapsulated electrode meet 465 ± 10 K and then decreases to a minimum of 345 ± 10 K as you go across the encapsulated electrode to the edge of the discharge. The vibrational temperature profile in Fig. 4 shows that the maximum vibrational temperature of 3250 K corresponds to the same spatial location as the maximum rotational temperature. The vibrational temperature is seen to decrease from the maximum value in the gap down to a minimum of 2850 K at the edge of the discharge.

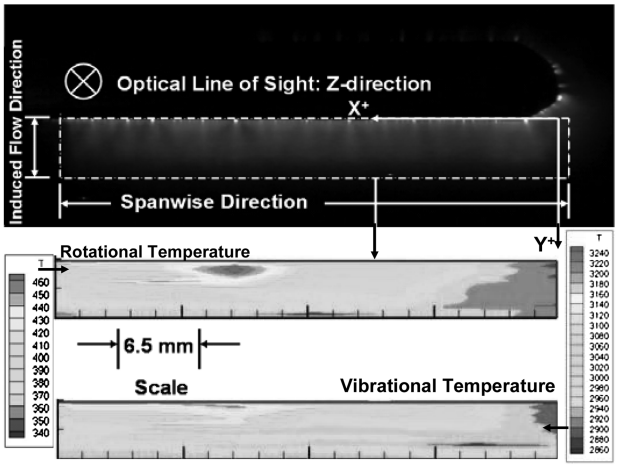

Fig. 4 The rotational temperature profile (top) and vibrational temperature profile (bottom) for the region of the discharge within the dashed box.

Figure 5 shows a comparison between the best-fit Boltzmann distribution and the actual measured relative distribution of the vibrational energy levels for the $C^3\Pi_u$ electronic state of N_2. It is seen that the actual distribution deviates from the Boltzmann distribution; however, this deviation is small and the vibrational distribution of the $C^3\Pi_u$ state can be approximated by a Boltzmann distribution.

These rotational and vibrational results also show nonuniform temperatures with large fluctuations in the spanwise direction. This is emphasized in the line profile plots in Figs. 6–8. Each line represents the rotational temperature (left figure) and vibrational temperature (right figure) along a constant y coordinate. Figure 6 shows these fluctuations have a maximum rotational and vibrational temperature of 460 and 3250 K at a y location of 0 mm (the edge of the exposed electrode) and then damp out in the induced flow direction. A prominent temperature peak occurs in the profiles between $0.14 \leq y \leq 0.82$ mm. It is also observed that the minimums and maximums of the rotational and vibrational temperature profiles correspond to the same location. Figure 7 shows the fluctuations for y coordinates from 1.0–2.5 mm. In this figure it is seen that the fluctuations are beginning to damp out. In Fig. 8, which shows the rotational and vibrational temperature line plots with y-coordinates between 2.5–4.0 mm, the fluctuations are completely gone as is the temperature gradient in the flow direction.

An explanation of the spatial variation of the rotational and vibrational temperatures can be obtained by visual observation of the discharge as shown in Fig. 9. This figure shows four successive images of the ASDBD separated in time by 30 s. Note, the attachment points of the microdischarges within the plasma (bright spots located

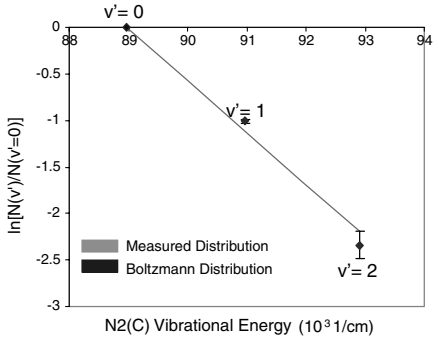

Fig. 5 The best-fit Boltzmann distribution of the measured vibrational distribution for the vibrational energy levels in the $C^3\Pi_u$ electronic state of N_2. The vibrational quantum number is indicated above the measured point.

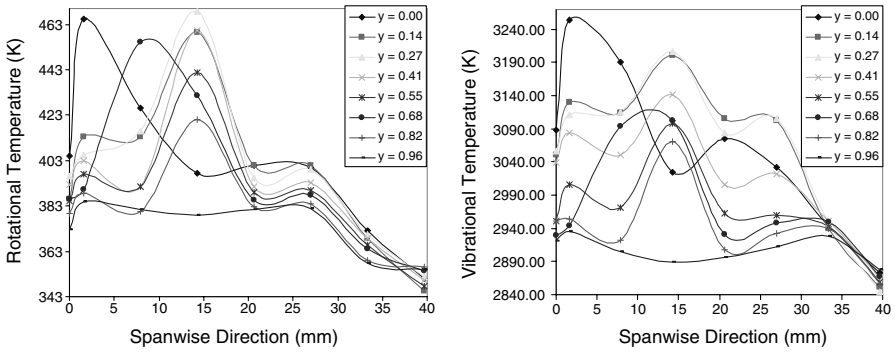

Fig. 6 Line plots of the rotational temperatures as a function of spanwise and flow direction for the first 1.0 mm across the encapsulated electrode. The error of each measured rotational and vibrational temperature is ±10 and ±300 K, respectively.

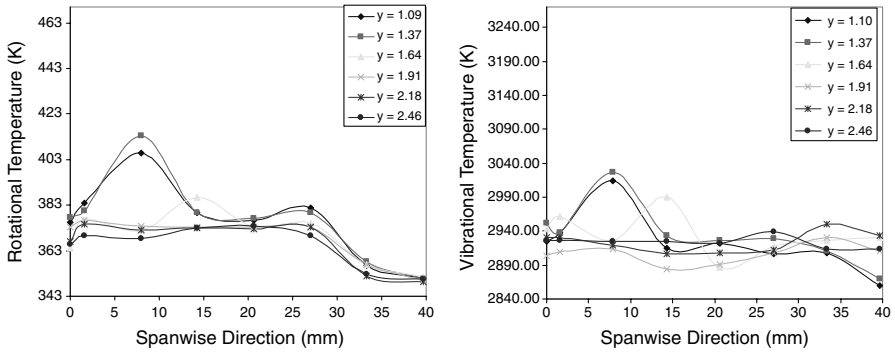

Fig. 7 Line plots of the rotational temperatures as a function of spanwise and flow directions for the 1.0–2.5 mm range across the encapsulated electrode. The error of each measured rotational and vibrational temperature is ±10 and ±300 K, respectively.

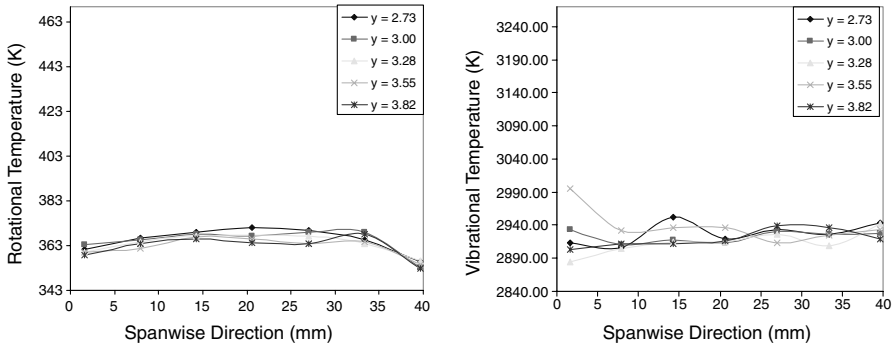

Fig. 8 Line plots of the rotational temperatures as a function of spanwise and flow directions for the 2.73–3.82 mm range across the encapsulated electrode. The error of each measured rotational and vibrational temperature is ±10 and ±300 K, respectively.

between the encapsulated and exposed electrode) remain approximately fixed spatially and appear to change only weakly with respect to time. In Fig. 6 the rotational temperature peaks occurring at $y = 14.1$ mm corresponds well with the attachment point in Fig. 9. Other local temperature maxima in the x direction correlate less strongly with the attachment points. Correlation with the alignment of the attachment points was done by shining a laser through the back side of the collection optics and noting the position of the line of sight.

These microdischarges may have some effect on the flow structure. Figure 10 shows PIV (particle image velocimetry) measurements from a similar ASDBD experiment that show spanwise periodic regions of higher and lower velocity within the induced flow [50]. These PIV results were obtained from a 2000 Hz square wave but were also evident for a 5000 Hz sine wave. In this experiment, the velocity fluctuations could not conclusively be correlated with attachment points in the discharge. The possibility remains that they may be due to fluid dynamic instabilities in the induced flow.

The next set of results, shown in Figs. 11–15, are for the same optical line of sight as the previously presented results. The rotational

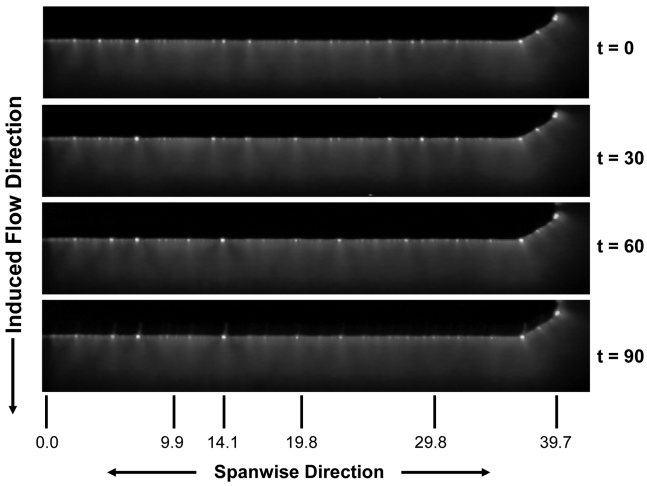

Fig. 9 Images of the DBD taken in 30 s intervals. The dimensions given in the spanwise direction are in millimeters.

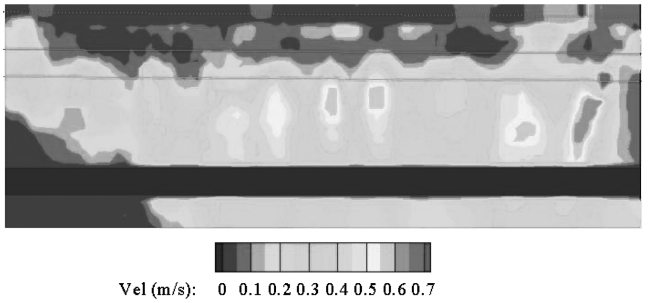

Fig. 10 Velocity contour plot obtained from PIV measurements for a square wave [50].

and vibrational temperatures are still obtained from the $C^3\Pi_u - B^3\Pi_g$ band system of N_2, and rotational temperatures for N_2^+ are obtained from the $B^2\Sigma_u^+ - X^2\Sigma_g^+$ electronic band system. In these results, only the line profile at $y = 0$ mm is measured. In addition, a new ASDBD had to be built for these results, but it was made so that the dimensions are the same as the first model. Even though the dimensions were kept the same, the attachment points of the microdischarges changed locations. It was observed that the location of the attachment points remained approximately in the same location as a function of time, as was the case with the first DBD. However, using new electrodes resulted in the observed fluctuations in temperature shifting to new locations.

Figure 11 shows the rotational temperatures for N_2 as a function of voltage. It is seen that the rotational temperature increases from a minimum of 320 ± 10 K to a maximum of 390 ± 10 K as the voltage is increased. The measurements again show fluctuations in the spanwise direction.

Figure 12 shows the corresponding rotational temperatures for N_2^+ for all four voltages at the same induced flow direction coordinate of 0 mm. The rotational temperature of N_2^+ also increases with increasing voltage from a minimum of 430 ± 15 K to a maximum of 760 ± 15 K. Figure 13 gives the corresponding vibrational temperatures, which range from 2380–2540 K. The rotational temperatures of N_2 and N_2^+ are seen to be drastically different from one another. The deviation in rotational temperatures increases as the voltage is increased. This was observed by obtaining the average temperature of each species for each voltage setting and then taking the difference. Figure 14 shows the relationship between the average temperature difference vs the discharge voltage. It should be noted that the rotational distribution of each species is well approximated by the Boltzmann distribution, as can be seen in Fig. 3.

Stefanovic et al. [42] found the same deviation in rotational temperature between $N_2(C^3\Pi_u \rightarrow B^3\Pi_g)$ and $N_2^+(B^2\Sigma_u^+ \rightarrow X^2\Sigma_g^+)$ for a parallel PDBD operating in dry air. The mechanism responsible, according to Stefanovic et al., is related to the populating kinetics. Stefanovic et al. argued that the lifetime of $N_2^+(B^2\Sigma_u^+)$ species is around 0.1 ns, and because the main production mechanism is

$$N_2(X^1\Sigma_g^+) + e \rightarrow N_2^+(B^2\Sigma_u^+) + 2e \tag{6}$$

the spontaneous emission of $N_2^+(B^2\Sigma_u^+ \rightarrow X^2\Sigma_g^+)$ occurs on a similar time scale as the lifetime, therefore only occurring during the active time of the microdischarge. The main production mechanism of $N_2(C^3\Pi_u)$, identified by Stefanovic et al., occurs from direct electron impact of the ground state and the energy pooling reaction

$$N_2(A^3\Sigma_u^+) + N_2(A^3\Sigma_u^+) \rightarrow N_2(C^3\Pi_u) + N_2(X^1\Sigma_g^+) \tag{7}$$

According to Stefanovic et al., the production of the metastable species $N_2(A^3\Sigma_u^+)$ is predominantly produced by recombination reactions, effectively delaying the emission of the $C^3\Pi_u \rightarrow B^3\Pi_g$ transition of N_2. This means that the emissions of these two electronic band systems occur at different times within the discharge. They performed a computational study of the Navier–Stokes equations to see if the gas temperature could change during this time and found that after the current pulse, a rapid jump in temperature and pressure occurred. They showed that the temperature change causes the gas to expand radially outward from the microdischarge on a time scale of 0.1–1 μs. This expansion process causes the gas temperature to drop. Stefanovic et al. argue that the deviation in temperature between the two emitting species occurs because spontaneous emission from the $N_2^+(B^2\Sigma_u^+ \rightarrow X^2\Sigma_g^+)$ electronic band system occurs predominantly before this expansion process when the gas

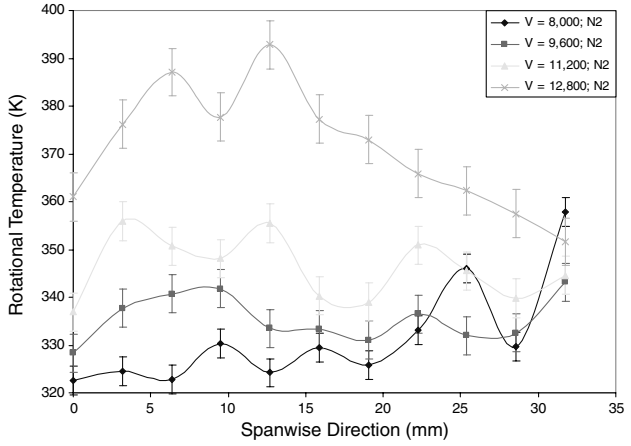

Fig. 11 Line plots of the rotational temperatures as a function of voltage at an induced flow direction coordinate of 0 mm for N_2.

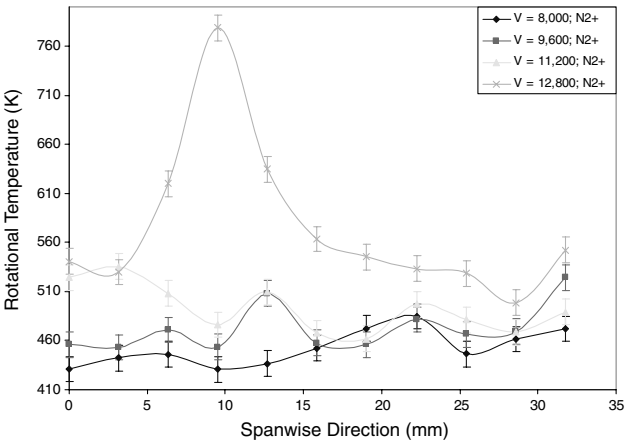

Fig. 12 Line plots of the rotational temperatures as a function of voltage at an induced flow direction coordinate of 0 mm for N_2^+.

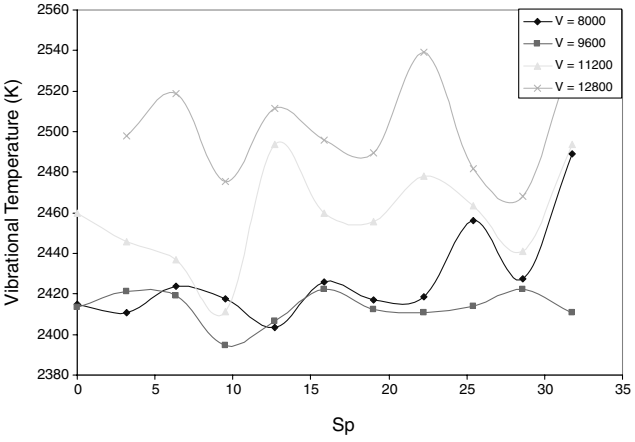

Fig. 13 Line plots of the vibrational temperatures as a function of voltage at an induced flow direction coordinate of 0 mm for the vibrational energy levels of the $C^3\Pi_u$ electronic state of N_2. The error of each measured temperature point is ±300 K.

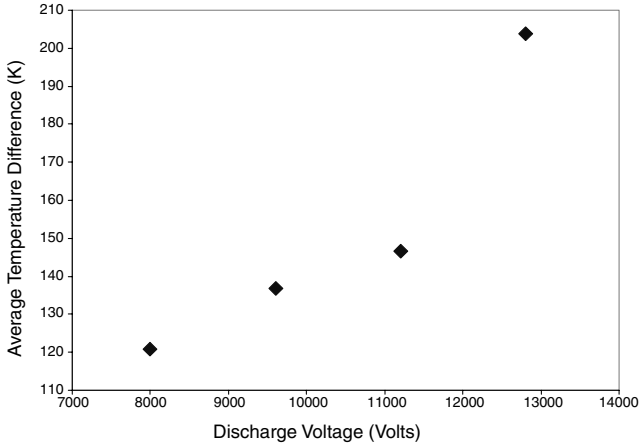

Fig. 14 The average rotational temperature difference between N_2 and N_2^+ vs the discharge voltage. It can be seen that the difference increases as the discharge voltage is increased.

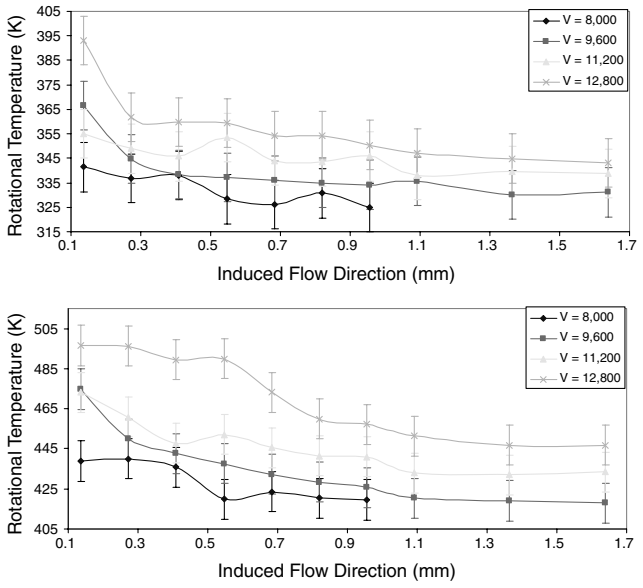

Fig. 15 Line plots of the rotational temperatures for N_2 (top) and N_2^+ (bottom) as a function of voltage in the induced flow direction.

temperature is hot; whereas the $N_2(C^3\Pi_u \rightarrow B^3\Pi_g)$ band system lags behind and emits after the expansion when the gas temperature is cooler. One problem with this explanation comes from Kozlov et al. [51] who shows that the spontaneous emission from $N_2^+(B^2\Sigma_u^+ \rightarrow X^2\Sigma_g^+)$ lags the emission from $N_2(C^3\Pi_u \rightarrow B^3\Pi_g)$ within an atmospheric pressure air PDBD by several nanoseconds. This is significantly smaller than the characteristic time of expansion and does not appear to be enough time for the microdischarge region to cool noticeably. Also, the emission of both transitions occurs at the same time current is flowing through the microdischarge. This would indicate that the microdischarge region is still heating when emission from $N_2(C^3\Pi_u - B^3\Pi_g)$ is occurring.

There is another possible explanation for the deviation in rotational temperature between N_2 and N_2^+. Some regions within the discharge, such as the sheath, are not effectively shielded by the discharge from the applied electric field. In these regions, ions could pick up extra energy from the electric field, and, although some of the energy is transferred to the neutrals, it may be possible for the two species to be out of equilibrium with each other. To conclusively determine the exact mechanism or mechanisms for the discrepancy in rotational temperatures requires more investigation.

The final results are shown in Fig. 15 and correspond to the rotational temperatures of N_2 and N_2^+ in the induced flow direction as a function of voltage. Results show the rotational temperatures of both species decrease in the induced flow direction and are again different from one another. The difference in temperature decreases slightly for each voltage as a function of increasing y coordinate.

VI. Conclusions

The rotational and vibrational temperature profiles for the discharge region of a pure air asymmetric surface mode dielectric barrier discharge have been spatially resolved in the induced flow direction, as a function of voltage, for N_2. The rotational temperature for N_2^+, within the discharge, has also been spatially resolved in the induced flow direction. The rotational temperature of N_2 ranged from 393 to 342 $\pm$ 10 K for a peak-to-peak voltage of 12,800 V and 341 to 325 $\pm$ 10 K for a peak-to-peak voltage of 8000 V in the induced flow direction. Similarly, N_2^+ ranged from 497 to 447 $\pm$ 15 K for a peak-to-peak voltage of 12,800 V and 439 to 420 $\pm$ 15 K for a peak-to-peak voltage of 8000 volts. The vibrational temperature ranged from 3250 to 2850 $\pm$ 300 K for a peak-to-peak voltage of 12,800 V. The reason for the discrepancy in rotational temperatures between the two species is still unknown, but a couple of possible explanations have been presented in this paper. The determination of the actual mechanism requires additional investigation.

In addition to resolving the rotational and vibrational temperature profiles for the discharge region of a pure air asymmetric surface mode dielectric barrier discharge in the induced flow direction, these temperatures have been spatially resolved in the spanwise direction also. Rotational temperature profiles, for both species, fluctuated in the spanwise direction, and these fluctuations damp in the induced flow direction. There appears to be some correlation between the attachment points of the microdischarges at the edge of the exposed electrode and local temperature fluctuations.

Acknowledgments

This work was funded through the U.S. Air Force Office of Scientific Research, under a laboratory task managed by John Schmisseur and through the Dayton Area Graduate Studies DAGSI/AFRL program. The authors are very grateful for this support. In addition, the authors also wish to thank the Air Force Research Laboratory, Air Vehicles Directorate Integration Branch, and General Dynamics for their support of laboratory operations and David Neff for his work on the voltage and current measurements.

References

[1] Enloe, C. L., McLaughlin, T. E., VanDyken, R. D., Kachner, K. D., Jumper, E. J., and Corke, T. C., "Mechanisms and Responses of a Single Dielectric Barrier Plasma Actuator: Plasma Morphology," *AIAA Journal*, Vol. 42, No. 3, 2004, pp. 589–594. doi:10.2514/1.2305

[2] Roth, J. R., Sherman, D. M., and Wilkinson, S. P., "Boundary Layer Flow Control with a One Atmosphere Uniform Glow Discharge Surface Plasma," AIAA Paper 98-0328, Jan. 1998.

[3] Huang, J., Corke, T. C., and Thomas, F. O., "Unsteady Plasma Actuators for Separation Control of Low-Pressure Turbine Blades," *AIAA Journal*, Vol. 44, No. 7, 2006, pp. 1477–1487. doi:10.2514/1.19243

[4] Post, M., and Corke, T., "Separation Control on High Angle of Attach Airfoil Using Plasma Actuators," *AIAA Journal*, Vol. 42, No. 11, 2004, pp. 2177–2184. doi:10.2514/1.2929

[5] Do, H., Kim, W., Mungal, M. G., and Cappeli, M. A., "Bluff Body Flow Separation Control Using Surface Dielectric Barrier Discharges," AIAA Paper 2007-939, Jan. 2007.

[6] Porter, C. O., McLaughlin, T. E., Enloe, C. L., Font, G. I., Roney, J., and Baughn, J. W., "Boundary Layer Control Using a DBD Plasma Actuator," AIAA Paper 2007-786, Jan. 2007.

[7] Vorobiev, A. N., Rennie, R. M., Jumper, E. J., and McLaughlin, T. E., "An Experimental Investigation of Lift Enhancement and Roll Control Using Plasma Actuators," AIAA Paper 2006-3383, 2006.

[8] McLaughlin, T. E., Munska, M. D., Vaeth, J. P., Dauwalter, T. E., Goode, J. R., and Siegel, S. G., "Plasma-Based Actuators for Cylinder

Wake Vortex Control," AIAA Paper 2004-2129, June 2004.
[9] McLaughlin, T. E., Felker, B., Avery, J. C., and Enloe, C. L., "Further Experiments in Cylinder Wake Modification with Dielectric Barrier Discharge Forcing," AIAA Paper 2006-1409, Jan. 2006.
[10] Wilkison, S. P., "Investigation of an Oscillating Surface Plasma for Turbulent Drag Reduction," AIAA Paper 2003-1023, Jan. 2003.
[11] Lopera, J., Ng, T. T., Patel, M. P., Vasudevan, S., and Corke, T. C., "Aerodynamic Control of 1303 UAV Using Windward Surface Plasma Actuators on a Separation Ramp," AIAA Paper 2007-636, Jan. 2007.
[12] Boeuf, J. P., and Pitchford, L. C., "Electrohydrodynamic Force and Aerodynamic Flow Acceleration in Surface Dielectric Barrier Discharge," *Journal of Applied Physics*, Vol. 97, No. 10, May 2005, pp. 652–662.doi: 10.1088/0022-3727/40/3/S03
[13] Font, G. I., "Boundary-Layer Control with Atmospheric Plasma Discharges," *AIAA Journal*, Vol. 44, No. 7, 2006, pp. 1572–1578. doi:10.2514/1.18542
[14] Font, G. I., Enloe, C. L., McLaughlin, T. E., and Orlov, D., "Plasma Discharge Characteristics and Experimentally Determined Boundary Conditions for a Plasma Actuator," AIAA Paper 2007-188, Jan. 2007.
[15] Font, G. I., Jung, S., Enloe, C. L., McLaughlin, T. E., Morgan, W. L., and Baughn, J. W., "Simulation of the Effects of Force and Heat Production by a Plasma Actuator on Neutral Flow Evolution," AIAA Paper 2006-167, Jan. 2006.
[16] Singh, K. P., Roy, S., and Gaitonde, D. V., "Modeling of Dielectric Barrier Discharge Plasma Actuator with Atmospheric Air Chemistry," AIAA Paper 2006-3381, June 2006.
[17] Likhanskii, A. V., Shneider, M. N., Opaits, D. F., Miles, R. B., and Macheret, S. O., "Numerical Modeling of DBD Plasma Actuators and the Induced Air Flow," AIAA Paper 2007-4533, June 2007.
[18] Likhanskii, A. V., Shneider, M. N., Macheret, S. O., and Miles, R. B., "Modeling of Dielectric Barrier Discharge Plasma Actuators Driven by Repetitive Nanosecond Pulses," *Physics of Plasmas*, Vol. 14, No. 7, 2007, pp. 073501–073509.doi:DOI:10.1063/1.2744227
[19] Orlov, D. M., Apker, T., He, C., Othman, H., and Corke, T. C., "Modeling and Experiment of Leading Edge Separation Control Using SDBD Plasma Actuators," AIAA Paper 2007-877, Jan. 2007.
[20] He, C., Corke, T. C., and Patel, M. P., "Numerical and Experimental Analysis of Plasma Flow Control Over a Hump Model," AIAA Paper 2007-935, Jan. 2007.
[21] Reasor, D. A., Jr., LeBeau, R. P., Jr., and Suzen, Y. B., "Unstructured Grid Simulations of Plasma Actuator Models," AIAA Paper 2007-3973, June 2007.
[22] Wang, C., and He, X., "Effect of Atmospheric Pressure Dielectric Barrier Discharge Air Plasma on Electrode Surface," *Applied Surface Science*, Vol. 253, No. 2, 2006, pp. 926–929. doi:10.1016/j.apsusc.2006.01.032
[23] Golubovskii, Y. B., Maiorov, V. A., Behnke, J., and Behnke, J. F., "Influence of Interaction Between Charged Particles and Dielectric Barrier Discharge in Nitrogen," *Journal of Physics D: Applied Physics*, Vol. 35, No. 8, 2002, pp. 751–761. doi:10.1088/0022-3727/35/8/306
[24] Choi, Y. H., Kim, J. H., and Hwang, Y. S., "One-Dimensional Discharge Simulation of Nitrogen DBD Atmospheric Pressure Plasma," *Thin Solid Films*, Vol. 26, May 2005, pp. 389–395.doi: 10.1016/j.tsf.2005.08.103
[25] Forte, M., Leger, L., Pons, J., Moreau, E., and Touchard, G., "Plasma Actuators for Airflow Control: Measurement of the Non-Stationary Induced Flow Velocity," *Journal of Electrostatics*, Vol. 63, No. 6-10, June 2005, pp. 929–936. doi:10.1016/j.elstat.2005.03.063
[26] Baughn, J. W., Porter, C. O., Peterson, B. L., McLaughlin, T. E., Enloe, C. L., Font, G. I., and Baird, C., "Momentum Transfer for an Aerodynamic Plasma Actuator with an Imposed Boundary Layer," AIAA Paper 2006-168, Jan. 2006.
[27] Opaits, D. F., Neretti, G., Likhanskii, A. V., Zaidi, S., Shneider, M. N., Miles, R. B., and Macheret, S. O., "Experimental Investigation of DBD Plasma Actuators Driven by Repetitive High Voltage Nanosecond Pulses with DC or Low-Frequency Sinusoidal Bias," AIAA Paper 2007-4532, June 2007.
[28] Porter, C. O., Baughn, J. W., McLaughlin, T. E., Enloe, C. L., and Font, G. I., "Temporal Force Measurements on an Aerodynamic Plasma Actuator," AIAA Paper 2006-104, Jan. 2006.
[29] Gregory, J. W., Enloe, C. L., Font, G. I., and McLaughlin, T. E., "Force Production Mechanisms of a Dielectric-Barrier Discharge Plasma Actuator," AIAA Paper 2007-185, Jan. 2007.
[30] Enloe, C. L., McLaughlin, T. E., Font, G. I., and Baughn, J. W., "Frequency Effects on the Efficiency of the Aerodynamic Plasma Actuator," AIAA Paper 2006-166, Jan. 2006.
[31] Enloe, C. L., McLaughlin, T. E., Font, G. I., and Baughn, J. W., "Parameterization of Temporal Structure in the Single-Dielectric-Barrier Aerodynamic Plasma Actuator," *AIAA Journal*, Vol. 44, No. 6, 2006, pp. 1127–1136. doi:10.2514/1.16297
[32] Enloe, C. L., McLaughlin, T. E., VanDyken, R. D., Kachner, K. D., Jumper, E. J., Corke, T. C., Post, M., and Haddad, O., "Mechanisms and Responses of a Single Dielectric Barrier Plasma Actuator: Geometric Effects," *AIAA Journal*, Vol. 42, No. 3, 2004, pp. 595–604. doi:10.2514/1.3884
[33] Enloe, C. L., McLaughlin, T. E., VanDyken, R. D., Kachner, K. D., Jumper, E. J., and Corke, T. C., "Mechanisms and Responses of a Single Dielectric Barrier Plasma Actuator: Plasma Morphology," *AIAA Journal*, Vol. 42, No. 3, 2004, pp. 589–594. doi:10.2514/1.2305
[34] Chiper, A. S., Anita, V., Agheorghiesei, C., Pohoata, V., Anita, M., and Popa, G., "Spectroscopic Diagnostics for a DBD Plasma in He/Air and He/N_2 Gas Mixtures," *Plasma Processes and Polymers*, Vol. 1, No. 1, 2004, pp. 57–62. doi:10.1002/ppap.200400003
[35] Bibinov, N. K., Fateev, A. A., and Wiesemann, K., "On the Influence of Metastable Reactions on Rotational Temperatures in Dielectric Barrier Discharges in He-N_2 Mixtures," *Journal of Physics D: Applied Physics*, Vol. 34, No. 12, 2001, pp. 1819–1826. doi:10.1088/0022-3727/34/12/309
[36] Luque, J., Kraus, M., Wokaun, A., Haffner, K., Kogelschatz, U., and Eliasson, B., "Gas Temperature Measurement in CH_4/CO_2 Dielectric-Barrier Discharges by Optical Emission Spectroscopy," *Journal of Applied Physics*, Vol. 93, No. 8, April 2003, pp. 4432–4438. doi:10.1063/1.1560570
[37] Motret, O., Hibert, C., Pellerin, S., and Pouvesle, J. M., "Rotational Temperature Measurements in Atmospheric Pulsed Dielectric Barrier Discharge-Gas Temperature and Molecular Fraction Effects," *Journal of Physics. D. Applied Physics*, Vol. 33, No. 12, 2000, pp. 1493–1498. doi:10.1088/0022-3727/33/12/311
[38] Pellerin, S., Musiol, K., Motret, O., Pokrzywka, B., and Chapelle, J., "Application of the (0, 0) Swan Band Spectrum for Temperature Measurements," *Journal of Physics. D. Applied Physics*, Vol. 29, No. 11, 1996, pp. 2850–2865. doi:10.1088/0022-3727/29/11/019
[39] Tomai, T., Katahira, K., Kubo, H., Shirmizu, Y., Sasaki, T., Noshizaki, N., and Terashima, K., "Carbon Materials Syntheses Using Dielectric Barrier Discharge Microplasma in Supercritical Carbon Dioxide Environments," *The Journal of Supercritical Fluids*, Vol. 41, No. 3, 2007, pp. 404–411. doi:10.1016/j.supflu.2006.12.003
[40] Nersisyan, G., and Graham, W. G., "Characterization of a Dielectric Barrier Discharge Operating in an Open Reactor with Flowing Helium," *Plasma Sources, Science and Technology*, Vol. 13, No. 4, 2004, pp. 582–587. doi:10.1088/0963-0252/13/4/005
[41] Borghi, C. A., Cristofolini, A., Carraro, M. R., and Neretti, G., "An Analysis of a Three Phase Flat Panel Uniform Barrier Discharge at Atmospheric Pressure," AIAA Paper 2006-3380, June 2006.
[42] Stefanovic, I., Bibinov, N. K., Deryugin, A. A., Vinogradov, I. P., Napartovich, A. P., and Wiesemann, K., "Kinetics of Ozone and Nitric Oxides in Dielectric Barrier Discharges in O_2/NO_x and $N_2/O_2/NO_x$ Mixtures," *Plasma Sources, Science and Technology*, Vol. 10, No. 3, 2001, pp. 406–416. doi:10.1088/0963-0252/10/3/303
[43] Biberman, L. M., Vorobev, V. S., and Yakuboy, I. T., *Kinetics of Nonequilibrium Low-Temperature Plasmas*, Consultants Bureau, New York, 1987, p. 388.
[44] Williamson, J., and DeJoseph, C., Jr., "Determination of Gas Temperature in an Open-Air Atmospheric Pressure Plasma Torch from Resolved Plasma Emission," *Journal of Applied Physics*, Vol. 93, No. 4, 2003, pp. 1893–1898. doi:10.1063/1.1536736
[45] Stanfield, S. A., Menart, J., Shang, J., Kimmel, R., and Hayes, J., "Application of a Spectroscopic Measuring Technique to Plasma Discharge in Hypersonic Flow," AIAA Paper 2006-0559, Jan. 2005.
[46] Herzberg, G., *Molecular Spectra and Molecular Structure I. Spectra of Diatomic Molecules*, Krieger, Malabar, FL, 1950, pp. 20, 204–207.
[47] Stanfield, S. A., Menart, J., DeJoseph, C., Kimmel, R., and Hayes, J., "Rotational and Vibrational Temperatures for a Dielectric Barrier Discharge in Air Using Emission Spectroscopy," AIAA Paper 2007-3876, June, 2007.
[48] Gilmore, F. R., Laher, R. R., Espy, P. J., "Franck-Condon Factors, *r*-Centroids, Electronic Transition Moments, and Einstein Coefficients

for Many Nitrogen and Oxygen Band Systems," *Journal of Physical and Chemical Reference Data*, Vol. 21, No. 5, 1992, pp. 1005–1107.

[49] Laher, R. R., and Gilmore, F. R., "Improved Fits for the Vibrational and Rotational Constants of Many States of Nitrogen and Oxygen," *Journal of Physical and Chemical Reference Data*, Vol. 20, No. 4, 1991, pp. 685–712.

[50] Kimmel, R. L., Estevadeordal, J., and Gogineni, S., "Characterization of Flow Generated by Dielectric Barrier Discharges (DBD)," *59th Annual Meeting of the American Physical Society Division of Fluid Dynamics*, Paper GH.00010, 2006.

[51] Kozlov, K. V., Wagner, H. E., Brandenburg, R., and Michel, P., "Spatio-Temporally Resolved Spectroscopic Diagnostics of the Barrier Discharge in Air at Atmospheric Pressure," *Journal of Physics. D. Applied Physics*, Vol. 34, No. 21, 2001, pp. 3164–3176. doi:10.1088/0022-3727/34/21/309

R. Lucht
Associate Editor